Resonant breakup of ^{8}Be in ^{112}Sn(^{7}Li,^{8}Be $\rightarrow 2\alpha$) reaction

D. Chattopadhyay,[1,2,*] S. Santra,[1,2] A. Pal,[1,2] A. Kundu,[1,2] K. Ramachandran,[1] R. Tripathi,[2,3] B. J. Roy,[1,2] Y. Sawant,[1] B. K. Nayak,[1,2] A. Saxena,[1,2] and S. Kailas[1,2]

[1]*Nuclear Physics Division, Bhabha Atomic Research Centre, Mumbai 400085, India*

[2]*Homi Bhabha National Institute, Anushakti Nagar, Mumbai 400094, India*

[3]*Radio Chemistry Division, Bhabha Atomic Research Centre, Mumbai 400085, India*

(Received 22 March 2018; revised manuscript received 15 June 2018; published 17 July 2018)

Background: Reactions involving weakly bound projectiles with $\alpha + x$ cluster structure are known to produce a large number of α particles, where transfer-induced breakup is one of the possible origins. Detailed investigation on each of these channels is desirable to understand the underlying reaction mechanism.

Purpose: Our purpose is to measure the $+1p$ transfer-induced breakup in the ^{112}Sn(^{7}Li,^{8}Be $\rightarrow 2\alpha$) reaction to understand the possible modes of ^{8}Be breakup and their contribution to inclusive α production.

Methods: α-α coincidence measurements have been carried out for the above reaction at $E_{\text{beam}} = 30$ MeV. Projectile-like fragments were detected using five sets of Si-strip-detector telescopes and five sets of single Si-detector telescopes. Optical model analysis of elastic scattering data, coupled reaction channels (CRC), and continuum discretized coupled channels (CDCC) calculations were performed to understand the measured cross sections.

Results: The experimental cross sections for $+1p$ transfer-induced breakup in (^{7}Li,^{8}Be $\rightarrow 2\alpha$) reaction through different resonance states of ^{8}Be have been obtained. Relative energy distribution and Monte Carlo simulation confirm the observation of breakup of ^{8}Be from its 4^{+} (11.35-MeV) resonant state for the first time along with its well-known 0^{+} (92-keV) and 2^{+} (3.12-MeV) resonances. Simultaneous description of elastic scattering, transfer, and breakup cross sections have been made using CDCC plus CRC formalism.

Conclusions: Production of α particles in $+1p$ transfer-triggered breakup is found to proceed mainly through three resonance (0^{+}, 2^{+}, and 4^{+}) states of ^{8}Be.

DOI: 10.1103/PhysRevC.98.014609

I. INTRODUCTION

The phenomena of enhancement in α-particle production and suppression in the complete fusion at above-barrier energies in reactions involving heavy targets with weakly bound projectiles such as ^{6}Li,^{7}Li, and ^{9}Be as compared to strongly bound projectiles are well known [1–24]. The low breakup threshold of the weakly bound nucleus, which is responsible for introducing the projectile breakup channels, is the primary reason for the above observations. The coupling of the breakup channels to the elastic channel gives rise to a repulsive polarization potential that increases the fusion barrier and thus reduces the complete fusion cross section [18,19], especially at above-barrier energies. Second, all the above projectiles have the $\alpha + x$ cluster structure, and they may directly or sequentially break into α and x fragments [25–32] while moving in the field of target nucleus, leading to a large α production. For example, in a reaction involving ^{7}Li, when the excitation energy is above the breakup threshold, it may directly break into $\alpha + t$ or inelastically get excited to one of its resonant states and subsequently break into $\alpha + t$. It may also happen that, by $1n$ ($2n$) stripping, the ^{7}Li may transform into ^{6}Li (^{5}Li) and then break into $\alpha + d$ ($\alpha + p$). Similarly, after $1p$ pickup (stripping), ^{7}Li forms ^{8}Be (^{6}He) and may subsequently break into $\alpha + \alpha$ ($\alpha + 2n$). Since, ^{5}Li and ^{8}Be are quasibound nuclei, they will immediately break into $\alpha + p$ and $\alpha + \alpha$ particles respectively but the breakup of ^{6}Li (into $\alpha + d$) and ^{6}He (into $\alpha + 2n$) occurs when they are formed with excitation energy above their respective breakup threshold. So, along with direct breakup, transfer-induced breakup is equally important not only for ^{7}Li but also for other weakly bound projectiles as observed in several studies [25–32] to understand different modes of projectile breakup and their consequences on α-particle production, fusion cross sections, and other observables. In addition to understanding the breakup reaction mechanism, the cross sections for the individual transfer-induced breakup channels provide correct coupling strengths required for realistic coupled-channels calculations to find their effects on elastic as well as fusion cross sections [33,34].

One of the dominant transfer-induced breakup processes in the reactions involving weakly bound projectiles (^{6}Li, ^{7}Li, and ^{9}Be) is the formation of ^{8}Be by transfer reaction followed by its breakup into two α particles. In a recent article by Carnelli *et al.* [35] on inclusive and exclusive measurements of α-particle production in a reaction involving a medium-mass target, i.e., ^{7}Li+^{144}Sm reaction, possible contributions from various channels to inclusive α yield has been discussed. The probability of $1p$ pickup by ^{7}Li followed by breakup of ^{8}Be

*dipayanchattopadhyay90@gmail.com

into $\alpha + \alpha$ has been observed and the cross section measured has been found to be negligible compared to other channels that are contributing to the total α yield. In another detailed measurement and study on the ^{6}Li+^{112}Sn [27] reaction, the $1d$ pickup by ^{6}Li forming ^{8}Be and its subsequent breakup into $\alpha + \alpha$ via its 0^+ (g.s.) and 2^+ resonance states have been observed. For the ^{7}Li+^{93}Nb system [28], Pandit *et al.* have observed that $1p$ pickup by ^{7}Li forms ^{8}Be, which in turn disintegrates into $\alpha + \alpha$ only through its ground state. Simpson *et al.*, in the study for the ^{7}Li+^{58}Ni reaction [30], observed the breakup of ^{8}Be into $\alpha + \alpha$ via its 2^+ as well as 0^+ resonance states. They have studied the proximity of the transfer-induced breakup in ^{7}Li+^{58}Ni [30] using a classical simulation of postbreakup acceleration and found that the breakup of ^{8}Be into 2α via its ground state occurs far away while receding from the target, whereas the breakup via its resonant state (2^+) occurs near the target. It also suggests that due to postbreakup Coulomb acceleration of the α fragments the relative energy distribution corresponding to 2^+ state becomes very broad and may merge with other excited states. It may be mentioned that the above measurement has been carried out at an energy below the Coulomb barrier where the effect of postbreakup Coulomb acceleration is expected to be higher compared to above-barrier beam energies.

The 2α cluster structure of ^{8}Be at its ground state (0^+) as well as other two resonance states at 3.12 (2^+) and 11.35 MeV (4^+) is well reflected by the values of the spectroscopic factors for $\langle {}^{8}\mathrm{Be}|\alpha + \alpha\rangle$ overlaps: $S(\mathrm{g.s.}) = 0.84$, $S(2^+) = 0.83$, and $S(4^+) = 0.75$ [36]. Since the third resonance state (4^+), like the other two states, has a good overlap between two α particles in the cluster [37], the breakup of ^{8}Be into two α via this state is also possible at favorable excitation energies. However, there is no experimental evidence reported so far on the observation of ^{8}Be breakup via the 4^+ resonance state, so it would be interesting to investigate experimentally the existence of ^{8}Be breakup via its third resonance state and compare it with the breakup probabilities via the 0^+ and 2^+ states.

In the present paper, the results of the exclusive measurements for 2α breakup of ^{8}Be produced in the reaction ^{112}Sn(^{7}Li,^{8}Be) at a beam energy of $E_{\mathrm{beam}} = 30$ MeV are presented. It may be pointed out that the present work deals with the measurements at an energy well above the Coulomb barrier where the effect of the postbreakup Coulomb acceleration is expected to be relatively smaller compared to the near or sub-barrier energy dealt in Ref. [30]. Differential cross sections for ^{8}Be breakup through its resonance states have been determined. A simultaneous description of these breakup cross sections along with the cross sections for elastic scattering and few transfer channels has been attempted through a common coupled-channels calculation.

The paper is organized as follows. The experimental details are given in Sec. II. The data analysis to obtain the results on relative energy distribution and simulation on detector efficiency are described in Sec. III. The methods used to obtain the results of the breakup cross sections are given in Sec. IV. Coupled-channels calculations to explain these cross sections are described in Sec. V. Finally, the summary and conclusions of the present investigation are given in Sec. VI.

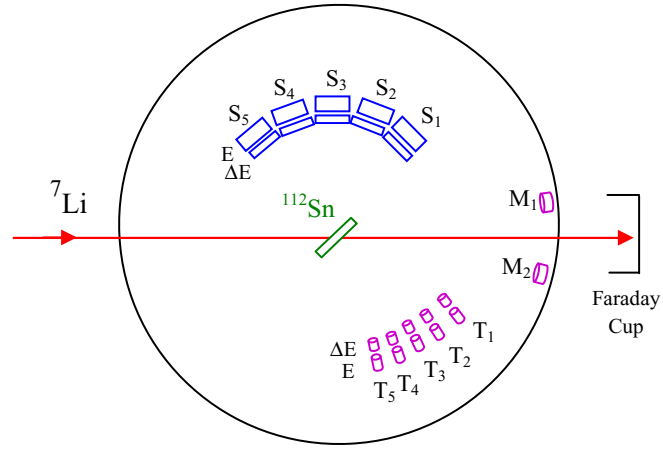

FIG. 1. The schematic diagram of the experimental setup showing strip detector array, single telescopes and monitors inside the scattering chamber.

II. EXPERIMENTAL DETAILS

Exclusive measurements have been carried out for ^{7}Li+^{112}Sn reaction at a beam energy $E_{\mathrm{beam}} = 30$ MeV, using the 14-UD Pelletron-Linac facility in Mumbai. Self-supporting enriched (>99%) ^{112}Sn foil of thickness ~540 μg/cm^2 was used as a target. The corrected beam energy with the loss in half target thickness is ≈29.8 MeV ($E_{\mathrm{c.m.}}/V_b \sim 1.37$). The cone angles [11] between two breakup fragments, i.e., $\alpha + \alpha$ through the ground as well as excited states of ^{8}Be are estimated to be in the range of ~6–70°. An array of strip detectors with large angular coverage was used to detect two α fragments in coincidence, produced by the breakup of ^{8}Be proceeding through the 0^+, 2^+, and 4^+ states. The schematic diagram of the experimental setup is shown in Fig. 1. Five strip telescopes (S_1–S_5) of Si strip detectors were placed on one of the two arms, at a distance of ~17.6 cm from the target center, inside a 1.5-m-diameter scattering chamber to detect the projectile-like fragments. Each strip telescope consists of two Si strip detectors (Micron Semiconductor W1 type), with thicknesses of ~60 μm (as ΔE) and ~1500 μm (as E) respectively. Each detector has 16 vertical strips in its front side and 16 horizontal strips in the back (with 256 pixels) covering an active area of 50 × 50 mm^2, with length and breadth of each strip being 50 and 3.1 mm respectively. Five such sets of strip telescopes placed side by side cover a total angular range of about ~93°. Two Si-surface barrier detectors (of thicknesses ~1000 μm) kept at ±20° were used to monitor the incident flux by measuring the Rutherford scattering. In addition, there were five single telescopes (T_1–T_5) of silicon surface barrier detectors (with $\Delta E \sim 50\,\mu$m, $E \sim 1000$–$2000\,\mu$m) placed on the second rotatable arm of the scattering chamber to measure the elastic scattering angular distribution covering a larger angular range. The typical inclusive two-dimensional spectrum of ΔE vs E obtained from a strip telescope as shown in Fig. 2 shows good separation of the particles with different masses (A = 1–7) and charges (Z = 1–3) produced by different reaction mechanisms. It was observed that an α detected in one pixel can be in coincidence with any of t, d, p,

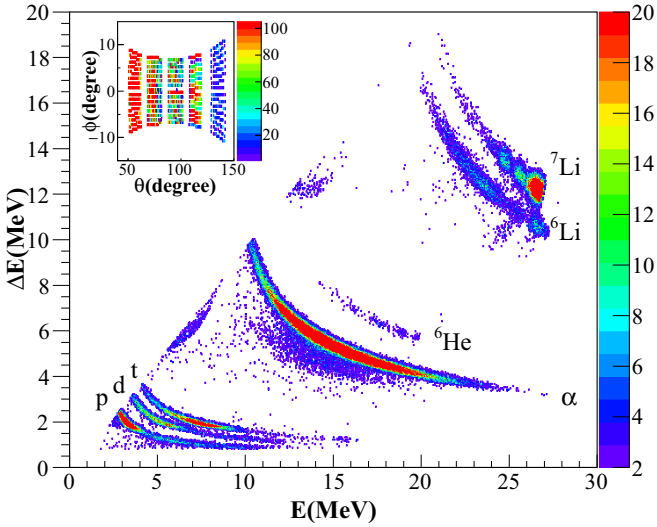

FIG. 2. Typical two-dimensional (ΔE vs E_{total}) energy calibrated spectrum acquired in one of the vertical strips at $\theta = 75^{\circ}$ for a beam energy of 30 MeV. The inset shows the total coverage in θ and ϕ by the strip detector array.

and α particles in another pixel, indicating the presence of direct, $-1n$, $-2n$, and $+1p$ triggered breakup, respectively. The $-1n$ and $-1p$ transfer reactions that survive posttransfer breakup produce ^{6}Li and ^{6}He respectively. Some of these events may also get generated in the direct breakup of ^{7}Li into ^{6}Li+n and ^{6}He+p, respectively, though with very low probabilities.

The inset of Fig. 2 shows the effective range of θ(∼51–142°) and ϕ(∼ ±7–11°) coverage of the strip detector array used in the present setup. The distribution of events shown in the figure corresponds to the actual number of α-α particles detected in coincidence by any two strips of all five strip telescopes without efficiency correction. The intensity distribution pattern shows a reduction in number of events as a function of increasing scattering angle (θ) as expected.

III. DATA ANALYSIS

A. Relative energy distribution

In the present work, we concentrate on (^{7}Li,^{8}Be), i.e., $1p$ pickup reaction followed by breakup into 2α particles. The coincidence yields in any two pixels with one of the α particles in one pixel and another α particle in any other pixel of another strip have been extracted independently by employing two-dimensional gates on respective α-particle bands of the spectra obtained from the strip telescopes. The relative energy distribution between two breakup fragments imply the excitation energy of the projectilelike nuclei above their breakup threshold through which the breakup occurs. With fragments of masses m_1 and m_2, the relative energy can be calculated from their individual energies E_1 and E_2 and the opening angle of their velocity vectors θ_{12}, as given by [38]

$$E_{\text{rel}} = \frac{m_2 E_1 + m_1 E_2 - 2\sqrt{m_1 m_2 E_1 E_2}\cos\theta_{12}}{m_1 + m_2}. \quad (1)$$

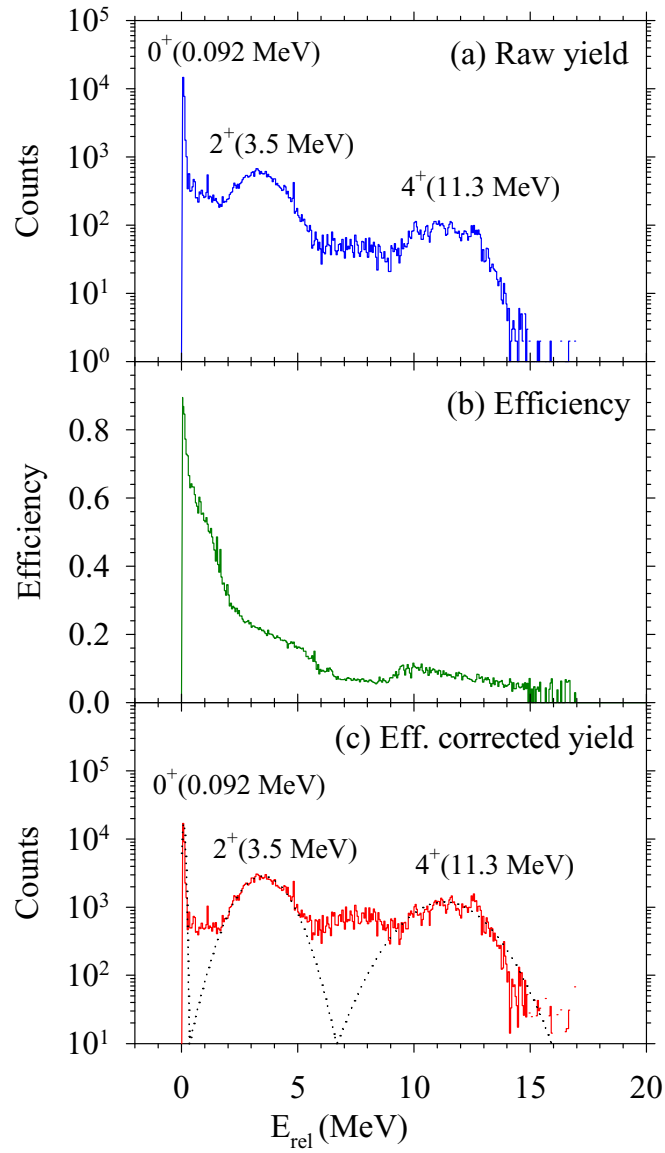

FIG. 3. Relative energy spectra corresponding to $\alpha + \alpha$ breakup channel at $E_{\text{beam}} = 30$ MeV, showing the breakup proceeding through different excitations of ^{8}Be. Dotted lines in panel (c) represent Gaussian fits to the resonance states to obtain the experimental peak positions and widths.

From the relative energy distribution without efficiency correction as shown in Fig. 3(a), it is observed that the breakup yield of $^{8}\text{Be} \rightarrow \alpha + \alpha$ peaks around 0.09, 3.5, and 11.3 MeV, corresponding to 0^{+}, 2^{+}, and 4^{+} states of ^{8}Be respectively.

To confirm that these peaks are not the artifacts due to modulations in efficiency of the detector array, a Monte Carlo simulation was carried out to obtain the relative energy-dependent efficiency as shown in Fig. 3(b). The nonsmooth behavior observed in the efficiency curve has arisen due to the inactive regions between two strip detectors and a few nonworking strips of some of the telescopes. In the simulation, the efficiency of detecting two breakup α fragments in coincidence by any two strips of the present strip detector array has been obtained as a function of E_{rel}. The breakup fragments were

TABLE I. The observed peak positions ($E_{\text{res.}}$) and widths ($\Gamma_{\text{res.}}$) for different resonance states compared with the ones from the literature [39].

State	$E^{\text{lit}}_{\text{res.}}$ (MeV)	$\Gamma^{\text{lit}}_{\text{res.}}$ (MeV)	$E^{\text{expt}}_{\text{res.}}$ (MeV)	$\Gamma^{\text{expt}}_{\text{res.}}$ (MeV)
0^+	0.092	0.0057	0.09	0.05
2^+	3.12	1.513	3.5	2.2
4^+	11.35	3.5	11.3	3.5

assumed to be emitted isotropically in the rest frame of the outgoing projectile-like nucleus before it broke up. The events with two breakup fragments falling on the same strip has been rejected. The relative energy and efficiency of the detector have been determined event by event. This efficiency distribution was applied to the raw data to obtain the efficiency corrected relative energy distribution as shown in Fig. 3(c). It confirms that the peak corresponding to 4^+ is indeed genuine. The observed peak positions and widths of all the three resonances (0^+, 2^+, and 4^+) obtained by Gaussian fits (dotted lines) are in reasonable agreement with the ones from the literature values [39] as compared in Table I. A small peaklike structure at $E_{\text{rel}} \sim 7.5$ MeV is possibly due to distortion in the relative energies of some of the events corresponding to the breakup of 2^+ and 4^+ states as they occur near the target [30]. However, the identification of the peaks at ~3.5 and ~11.3 MeV with their respective widths corresponding to 2^+ and 4^+ resonances is unambiguous.

Though the breakup of ^{8}Be through its 0^+ and 2^+ states have been observed in some of the earlier studies [27,30], to our knowledge, the breakup via its 4^+ resonance state is observed for the first time in the present measurement.

B. E_{rel} versus E_α

The relative energy distribution described above corresponds to the coincident two α fragments detected in all possible angles. The breakup via three resonant states can also be identified by plotting the relative energy E_{rel} versus fragment energy E_α of the events when two fragments detected at a particular angular difference $\Delta\theta(=\theta_1-\theta_2)$. For example, if $\Delta\theta > 50^\circ$ then only the events corresponding to 4^+ resonance state will be observed as the cone angles for other two resonant states are smaller. At smaller angular difference, e.g., $\Delta\theta \sim 2^\circ$, only 0^+ events will be observed, because one of the α fragments (which is backward moving) corresponding to 2^+ and 4^+ breakup will have energy ~1.5–7.5 MeV, smaller than the detector threshold (~8.5 MeV), and will be stopped in the ΔE detector without giving a coincident event in the two-dimensional ΔE-E plot. However, events corresponding to nonresonant breakup with relative energies lying between that of 0^+ and 2^+ states, though negligible, may be observed. Similarly, for $\Delta\theta \sim 35^\circ$, the events corresponding to only 2^+ will be observed because (i) the events corresponding to 0^+ state cannot be emitted as $\Delta\theta$ is beyond its cone angle (~6°) and (ii) for 4^+ breakup, the backward-moving α fragment with energy (~2–3 MeV) smaller than the detector threshold will be stopped in the ΔE detector.

Typical plots of E_{rel} versus E_α corresponding to $\Delta\theta$ equal to 2°, 35°, and 68° are shown in Figs. 4(a), 4(c), and 4(e) respectively. The corresponding one-dimensional projections on E_α are shown as black lines in Figs. 4(b), 4(d), and 4(f) respectively. The dotted lines represent relative energies corresponding to three resonance states. The solid black lines represent theoretical E_{rel} versus E_α obtained from kinematics. It can be observed that the measured events follow the kinematics very well, and the relative energies of the maximum number of events detected in each of the three different sets of θ_1 and θ_2 correspond to the breakup of only one of the resonance states. Because the width of the 0^+ resonance is smaller, two peaks in E_α (corresponding to forward-moving and backward-moving α) have been clearly observed in Fig. 4(b). However, for 2^+ and 4^+ resonances, the E_α distribution shows no peak as the width of these resonances are much larger, leading to a broad distribution.

Further, to confirm that the above distributions correspond to three resonant breakups, the results of the Monte Carlo simulations using the present detector geometry on E_α distributions corresponding to three separate resonant breakups have also been compared with the measured events distribution in Figs. 4(b), 4(d), and 4(f). The simulation has considered proper resonance widths as given in Table I. The peak positions and the widths of the resonances have been incorporated in the simulations by generating Gaussian distributions using the Box-Muller method. The simulated counts have been normalized and compared with the experimental data. A good agreement in the shapes between the simulation (red lines) and measured data (black lines) on E_α distributions confirms that these events indeed correspond to the breakup of ^{8}Be through its 0^+, 2^+, and 4^+ states respectively.

IV. 2α BREAKUP CROSS SECTIONS

Finally, the experimental differential cross sections of the transfer channel followed by breakup, i.e., $^7\text{Li} \rightarrow {}^8\text{Be} \rightarrow \alpha + \alpha$ through its 0^+, 2^+, and 4^+ resonance states have been obtained as follows. Using events reconstruction, a distribution of events corresponding to different θ,ϕ of ^{8}Be was generated. Now, for each $\theta(^8\text{Be})$ bin, the efficiency-corrected relative energy distribution $[Y_i^{\text{eff}}(\theta) = Y_i^{\text{raw}}(\theta)/\zeta_i]$ was obtained by summing over all $\phi(^8\text{Be})$ coverage of detector array corresponding to same $\theta(^8\text{Be})$ bin. Here, $Y_i^{\text{raw}}(\theta)$ represents the yield of the ith bin of the relative energy between ϵ_i and $\epsilon_i + d\epsilon_i$ without efficiency correction and ζ_i is the efficiency of the detector array for the same relative energy bin. For a particular θ bin, the coincidence yields under the peaks corresponding to 0^+, 2^+, and 4^+ states in relative energy distribution have been extracted individually by integrating $Y_i^{\text{eff}}(\theta)$ in steps of $d\epsilon_i$ over the respective relative energy range ($\Delta\epsilon = N d\epsilon_i$). Differential breakup cross sections for each of the resonance states is extracted from the following relation,

$$\frac{d\sigma^{br}}{d\Omega}(\theta) = \frac{\sum_{i=1}^{N} Y_i^{\text{eff}}(\theta)}{Y_{el}(\theta)} \frac{d\sigma^{el}}{d\Omega}(\theta), \tag{2}$$

where $Y_{el}(\theta)$ is the yield of elastic scattering in the solid angle corresponding to the element $\Delta\theta(^8\text{Be})$, $\Delta\phi(^8\text{Be})$, and

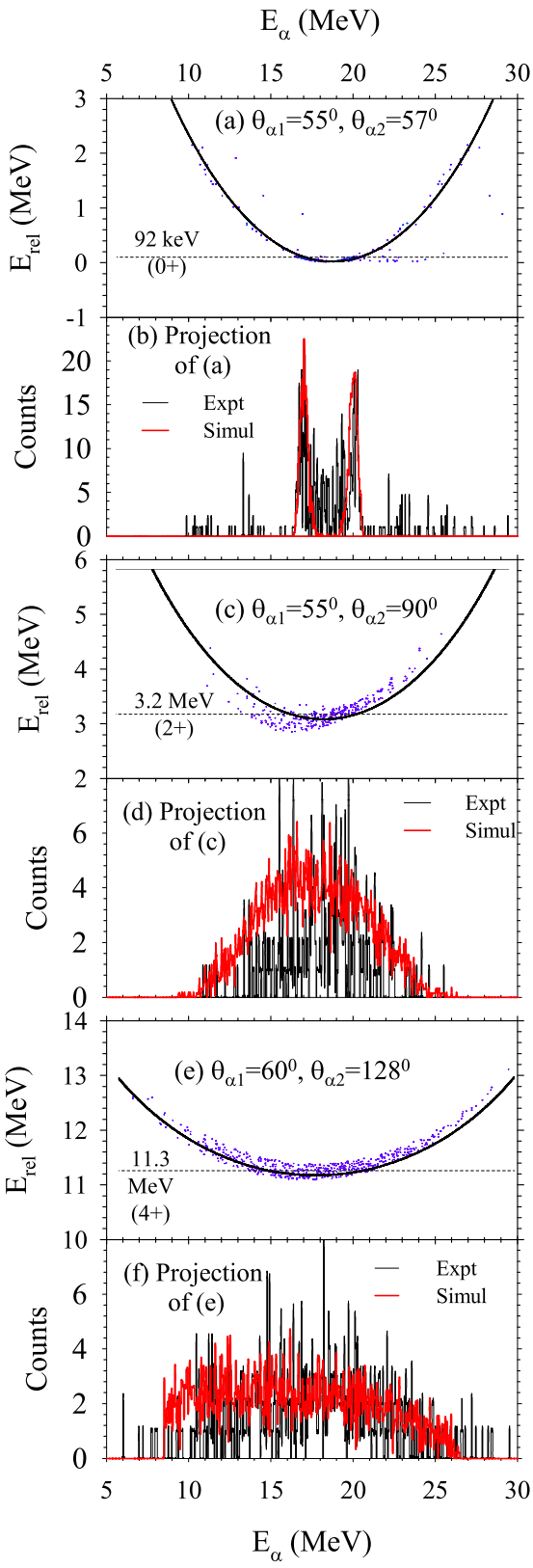

FIG. 4. Typical plots of $E_{\rm rel}$ versus E_α corresponding to the events when two α fragments detected at (a) $\theta_1 = 55^\circ$ and $\theta_2 = 57^\circ$, (c) $\theta_1 = 55^\circ$ and $\theta_2 = 90^\circ$, and (e) $\theta_1 = 60^\circ$ and $\theta_2 = 128^\circ$ respectively. Respective one-dimensional projections of the above events on E_α are given in panels (b), (d), and (f).

$\frac{d\sigma^{el}}{d\Omega}(\theta)$ is the differential elastic scattering cross section. The latter was obtained by normalizing (i) $Y_{el}(\theta)$ to the monitor yield $Y_m(\theta_m)$ corresponding to Rutherford scattering and (ii) their solid angles. The differential breakup cross sections thus obtained for 0^+, 2^+, and 4^+ states of ^{8}Be include the events corresponding to all possible target excitations and are shown as filled circles in Figs. 5(a), 5(b), and 5(c) respectively. The breakup cross sections for 0^+, 2^+, and 4^+ states are in decreasing order as expected. Although the breakup cross section via 0^+ and 2^+ states of ^{8}Be have been measured and described earlier, the cross section for 4^+ state is measured for the first time.

Because of so many closely spaced low-lying energy levels of the residual target nucleus ^{111}In, it is possible to have the 2α breakup events associated with a large number of target excitations, particulary for 0^+ and 2^+ breakup, but it is difficult to identify the events corresponding to individual excitations. It is also difficult to include so many target excitations in the coupled reaction channels (CRC) calculations due to the computation limitation leading to difficulty in comparing the experimental total 2α breakup with the theory. However, the events corresponding to no target excitation can be easily identified from the $E_{\rm rel}$ versus Q-value distribution plot (not shown here). So, the breakup cross sections for these events have been extracted separately and are shown as hollow circles in the respective figures. Dashed lines represent the results of CRC calculations (described in the next section) corresponding to the target being in the ground state. In order to compare the shape of the experimental total breakup cross sections with theory, a few representative states of low-lying target excitations have been included in the CRC couplings. Solid lines represent the sum of the cross sections corresponding to the ground state and all the excitations of the target that have been included in the calculations. The measured elastic scattering angular distribution has been shown as open diamonds in Fig. 5(d). The solid lines in Figs. 5(a)–5(d) represent the results from CRC calculations. The details of the CRC calculations have been given in Subsec. V A.

V. FRESCO CALCULATIONS

Coupled channels calculations using FRESCO (version 2.9) [40] have been performed to understand the above experimental breakup cross sections. Two sets of calculations have been carried out. First, only the CRC calculations have been made where no projectile breakup coupling is considered. However, the optical model potentials, obtained from the fit to the measured elastic scattering angular distribution, has been used for the entrance (elastic) channel. This may be considered as the local equivalent potential (i.e., bare + polarization potential) that has taken care of the effect of couplings of breakup and other direct reaction channels on elastic.

In the second case, both the continuum discretized coupled channels (CDCC) as well as the CRC calculations have been carried out using a bare potential in order to find the effect of couplings of breakup and other direct reaction channels on elastic and perform a simultaneous analysis of projectile breakup and transfer channels. Details of these calculations have been described in two separate sections as follows.

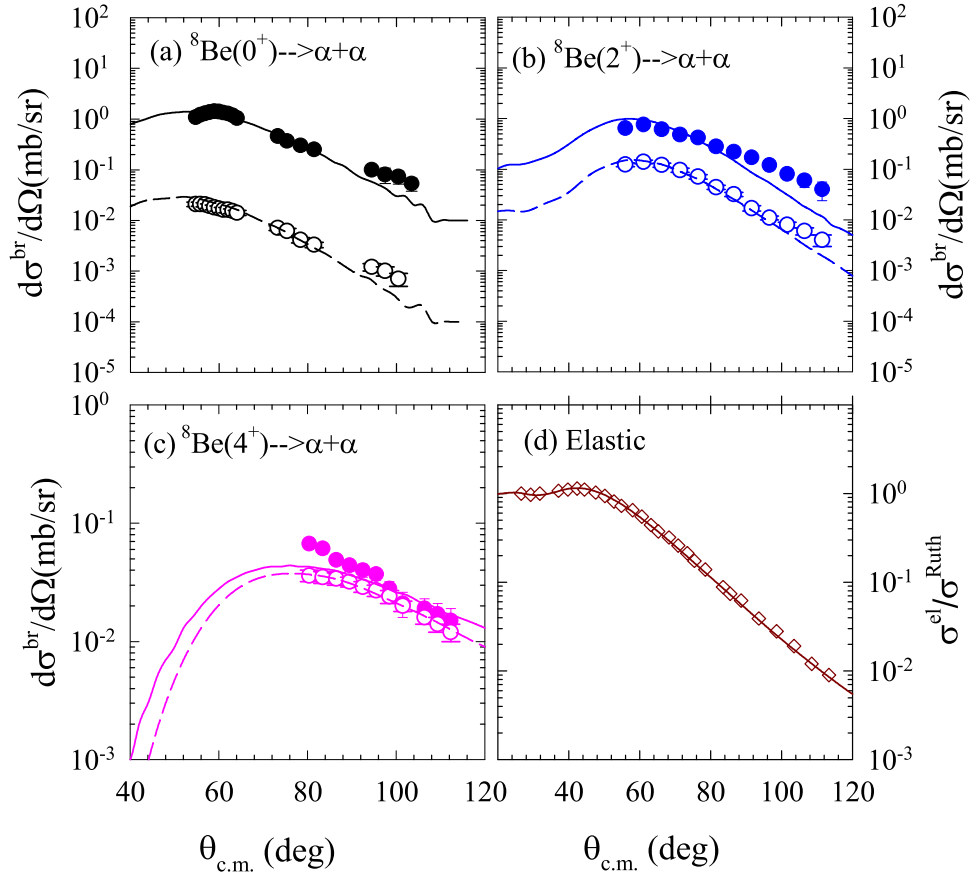

FIG. 5. Differential cross sections in center-of-mass frame for sequential breakup of ^{7}Li → ^{8}Be → $\alpha + \alpha$ corresponding to (a) 0^+, (b) 2^+, and (c) 4^+ states of ^{8}Be along with (d) the elastic scattering, measured at $E_{\text{beam}} = 30$ MeV. The hollow circles in panels (a), (b), and (c) represent 2α breakup cross sections corresponding to no target excitation, whereas the filled circles represent total breakup cross sections corresponding to both ground state as well as excited states of the target like nuclei. Lines represent the results of the CRC calculations using FRESCO. Dashed lines represent the theoretical cross sections only for g.s. to g.s transition and solid lines represent total cross sections for g.s. and excited states of ^{111}In.

A. CRC calculations

The $1p$ pickup, i.e., (^{7}Li,^{8}Be), reaction is known to be one of the most dominant breakup channels responsible for large α-particle production. The present work is focused on the exclusive measurements of 2α breakup of ^{8}Be which is produced in $1p$ pickup reaction. The ^{8}Be formed in this reaction being unstable, the $1p$ transfer cross-section is assumed to be equal to the breakup cross-section of ^{8}Be into 2α. It is possible that one of the two breakup α particles or the ^{8}Be itself may get absorbed by the target nucleus and thus reducing the outgoing flux. An imaginary potential used for the exit channel takes into account the above reduction in the outgoing flux. Thus, the $+1p$ transfer cross sections to be obtained from the CRC calculations should be comparable to the measured 2α breakup cross sections.

In the present CRC calculations, only two mass partitions (with ^{7}Li and ^{8}Be as ejectiles) have been considered. In the elastic-inelastic mass partition, both ^{7}Li and ^{112}Sn have been considered to be in ground state. The second mass partition corresponds to $1p$ pickup, i.e., (^{7}Li,^{8}Be) reaction. In this mass partition, the outgoing channels included in the couplings correspond to 0^+, 2^+, and 4^+ states of ^{8}Be, and the ground state $(9/2^+)$ plus 25 excited states of ^{111}In as listed in Table II. When ^{8}Be is in g.s., all the target excitations have been assumed to be possible, but for 2^+ and 4^+ excitations of ^{8}Be only the g.s. plus two excitations of ^{111}In have been considered. The details of the states coupled including the spectroscopic information and the spectroscopic amplitudes for the overlaps $\langle ^8\text{Be}|^7\text{Li} + p\rangle$ and $\langle ^{112}\text{Sn}|^{111}\text{In} + p\rangle$ used in the CRC calculations are given in Table II.

The real and imaginary potentials of Woods-Saxon volume form with $V_0 = 25.33$ MeV, $r_0 = 1.185$ fm, $a_0 = 0.75$ fm, $W_0 = 25.38$ MeV, $r_w = 1.17$ fm, and $a_w = 0.787$ fm, obtained from the optical model fit to the measured elastic scattering angular distribution have been used for the elastic-inelastic mass partition. For the transfer mass partition, the real part of the optical potential was same as that of the entrance channel mass partition but the imaginary part was taken to be of short-range Wood-Saxon square form with $W_0 = 10.00$ MeV, $r_w = 1.00$ fm, and $a_w = 0.4$ fm. The binding potentials for $p + ^7$Li are taken to be real and also of Woods-Saxon volume form with $V_0 = 50.0$ MeV, $r_0 = 1.15$ fm, $a_0 = 0.57$ fm,

TABLE II. Structure information and spectroscopic amplitudes (SA) for the overlaps $A = C + x$ (with binding energy BE) corresponding to different states of the nuclei A, C, and x used in the CRC calculations for (^{7}Li,^{8}Be) reaction.

Nucleus (A)	C	x	BE (MeV)	$nlj(x)$	SA
^{8}Be(0^{+})	^{7}Li (g.s., $3/2^{-}$)	p	17.255	$1p_{3/2}$	1.00
^{8}Be(2^{+})	^{7}Li (g.s., $3/2^{-}$)	p	14.135	$1p_{3/2}$	1.00
^{8}Be(4^{+})	^{7}Li (g.s., $3/2^{-}$)	p	5.905	$1f_{5/2}$	0.80
^{8}Be(4^{+})	^{7}Li (g.s., $3/2^{-}$)	p	5.905	$1f_{7/2}$	0.80
^{112}Sn(0^{+})	^{111}In (g.s., $9/2^{+}$)	p	7.560	$1g_{9/2}$	0.87
^{112}Sn(0^{+})	^{111}In (0.537 MeV, $1/2^{-}$)	p	7.023	$2p_{1/2}$	0.87
^{112}Sn(0^{+})	^{111}In (0.803 MeV, $3/2^{-}$)	p	6.757	$2p_{3/2}$	0.87
^{112}Sn(0^{+})	^{111}In (1.185 MeV, $1/2^{+}$)	p	6.375	$3s_{1/2}$	0.87
^{112}Sn(0^{+})	^{111}In (1.217 MeV, $5/2^{+}$)	p	6.343	$2d_{5/2}$	0.87
^{112}Sn(0^{+})	^{111}In (1.279 MeV, $5/2^{+}$)	p	6.281	$2f_{5/2}$	0.87
^{112}Sn(0^{+})	^{111}In (1.345 MeV, $3/2^{+}$)	p	6.215	$2d_{3/2}$	0.87
^{112}Sn(0^{+})	^{111}In (1.500 MeV, $7/2^{-}$)	p	6.060	$1g_{7/2}$	0.87
^{112}Sn(0^{+})	^{111}In (1.610 MeV, $9/2^{-}$)	p	5.950	$1g_{9/2}$	0.87
^{112}Sn(0^{+})	^{111}In (1.752 MeV, $9/2^{-}$)	p	5.808	$1g_{9/2}$	0.87
^{112}Sn(0^{+})	^{111}In (1.866 MeV, $1/2^{+}$)	p	5.694	$3s_{1/2}$	0.87
^{112}Sn(0^{+})	^{111}In (1.919 MeV, $3/2^{+}$)	p	5.641	$2d_{3/2}$	0.87
^{112}Sn(0^{+})	^{111}In (2.085 MeV, $1/2^{+}$)	p	5.475	$3s_{1/2}$	0.87
^{112}Sn(0^{+})	^{111}In (2.200 MeV, $5/2^{+}$)	p	5.360	$2d_{5/2}$	0.87
^{112}Sn(0^{+})	^{111}In (2.292 MeV, $3/2^{+}$)	p	5.268	$2d_{3/2}$	0.87
^{112}Sn(0^{+})	^{111}In (2.361 MeV, $9/2^{-}$)	p	5.199	$1g_{9/2}$	0.87
^{112}Sn(0^{+})	^{111}In (2.529 MeV, $5/2^{+}$)	p	5.031	$2d_{5/2}$	0.87
^{112}Sn(0^{+})	^{111}In (2.616 MeV, $3/2^{+}$)	p	4.944	$2d_{3/2}$	0.87

$V_{so} = 5.5$ MeV, $r_{so} = 1.15$ fm, $a_{so} = 0.57$ fm, where the subscript "*so*" corresponds to the spin-orbit term. The depth is automatically varied to reproduce the binding energy. Similarly the binding potential parameters used for $p + {}^{111}$In are $V_0 = 50.0$ MeV, $r_0 = 1.23$ fm, $a_0 = 0.65$ fm, $V_{so} = 6.0$ MeV, $r_{so} = 1.23$ fm, and $a_{so} = 0.65$ fm.

Because of the presence of so many closely spaced low-lying excited states of ^{111}In within the measured energy range, the cross sections corresponding to each of the target excitations could not be extracted. Also, in CRC calculations it was not possible to include all these excitations. So, the measured total 2α breakup cross sections corresponding to all these states cannot be compared with the calculations that have included only a limited number of excitations. However, the breakup yields corresponding to 0^{+}, 2^{+}, and 4^{+} states of ^{8}Be with no target excitation are reasonably clean, and the corresponding cross sections have been extracted separately and compared with the CRC results. The dashed lines in Fig. 5 represent the calculations assuming target in the ground state and they reproduce the experimental data reasonably well.

B. CDCC plus CRC calculations

To investigate the effect of projectile breakup and other direct reaction channels on elastic scattering simultaneously, the CDCC as well as CRC calculations using FRESCO have been carried out. Both the transfer channels and the inelastic (bound and unbound) excitations of the projectile have been coupled simultaneously. For the elastic-inelastic mass partition, the included channels correspond to projectile ground state, bound excited state (0.48 MeV, $1/2^{-}$), resonant states at 4.63 MeV ($7/2^{-}$) and 6.67 MeV ($5/2^{-}$), and nonresonant continuum above breakup threshold up to an excitation energy of about 8 MeV of ^{7}Li. No target excitation was considered. The projectile ^{7}Li has been assumed to have a two-body cluster structure of $\alpha + t$ with the breakup threshold ($E_{\rm th}$) of 2.47 MeV. The continuum of the α-t cluster of ^{7}Li at $E > E_{\rm th}$ has been discretized with respect to the α-t relative momentum of $\hbar k$ into several momentum bins, in steps of $\Delta k = 0.2$ fm^{-1}, up to $k = 0.8$ fm^{-1}[34]. Each bin has been treated as an excited state of α-t cluster with excitation energy equal to the mean excitation. An average wave function, assumed to be independent of energy within the bin width, has been normalized to unity. The spin of the excited state has been obtained as the vector sum of the α-t relative angular momentum L and the spin of the triton S. All possible states with $L = 0,1,2,3$ have been included. The binning of the continuum with $L = 3$ has been suitably modified to include the resonance states $7/2^{-}$ and $5/2^{-}$ with

TABLE III. The states of the projectile ^{7}Li included in the model space of the CDCC calculations. E_x, $E_{\rm min}$, and $E_{\rm max}$ respectively represent the mean, minimum, and maximum excitation energies of a particular bin state above the α-t breakup threshold.

L	I^{π}	E_x (MeV)	$E_{\rm min}$ (MeV)	$E_{\rm max}$ (MeV)
0	$1/2^{+}$	0.2421	0.0021	0.4821
0	$1/2^{+}$	1.2103	0.4841	1.9365
0	$1/2^{+}$	3.1470	1.9365	4.3570
0	$1/2^{+}$	6.0520	4.3570	7.7460
1	$3/2^{-}$	−2.47 (ground state)		
1	$3/2^{-}$	0.2421	0.0021	0.4821
1	$3/2^{-}$	1.2103	0.4841	1.9365
1	$3/2^{-}$	3.1470	1.9365	4.3570
1	$3/2^{-}$	6.0520	4.3570	7.7460
1	$1/2^{-}$	−1.99 (bound inelastic)		
1	$1/2^{-}$	0.2421	0.0021	0.4821
1	$1/2^{-}$	1.2103	0.4841	1.9365
1	$1/2^{-}$	3.1470	1.9365	4.3570
1	$1/2^{-}$	6.0520	4.3570	7.7460
2	$5/2^{+}$	0.2421	0.0021	0.4821
2	$5/2^{+}$	1.2103	0.4841	1.9365
2	$5/2^{+}$	3.1470	1.9365	4.3570
2	$5/2^{+}$	6.0520	4.3570	7.7460
2	$3/2^{+}$	0.2421	0.0021	0.4821
2	$3/2^{+}$	1.2103	0.4841	1.9365
2	$3/2^{+}$	3.1470	1.9365	4.3570
2	$3/2^{+}$	6.0520	4.3570	7.7460
3	$7/2^{-}$	0.2421	0.0021	0.4821
3	$7/2^{-}$	1.272	0.4840	2.0600
3	$7/2^{-}$	2.1600	2.0600	2.2600
3	$7/2^{-}$	3.2900	2.2600	4.3200
3	$5/2^{-}$	0.2421	0.0021	0.4821
3	$5/2^{-}$	1.2103	0.4841	1.9365
3	$5/2^{-}$	2.3200	1.9370	2.7100
3	$5/2^{-}$	4.2100	2.7100	5.7100

TABLE IV. The α-t binding potentials of Gaussian shape of the form $V = -V_0 e^{-r^2/a_0^2} + V_{so} e^{-r^2/a_{so}^2}$ used in the CDCC calculations.

State	V_0 (MeV)	a_0 (fm)	V_{so} (MeV)	a_0 (fm)
g.s. + nonresonant	83.78	2.520	2.006	2.520
bound inelastic	82.78	2.280	2.006	2.280
$7/2^-$ resonance	84.45	2.520	2.006	2.520
$5/2^-$ resonance	83.77	2.441	2.006	2.441

average excitation energies of 2.16 and 4.21 MeV, and widths of 0.2 and 3.0 MeV respectively. The model spaces of ^{7}Li that include the discretized states with mean excitation energy E_x and minimum to maximum excitation energy ($E_{\min}$ to $E_{\max}$) of the corresponding bins are enlisted in Table III.

The CDCC calculations were performed using cluster-folded (CF) interaction, where Sao-Paolo potentials [41] multiplied by 0.65 were used as the real parts of the fragment-target ($\alpha + ^{112}$Sn and $t + ^{112}$Sn) potentials. The imaginary potential for $\alpha + ^{112}$Sn was taken from Ref. [42], including both volume and surface terms, and for $t + ^{112}$Sn it has been calculated from the global optical model [43]. The α-t binding potentials of Ref. [44], suitably modified for resonances that generate proper phase shifts, have been used (see Table IV).

Along with the CDCC calculations that include the projectile excitations described above, the CRC calculations have also been performed simultaneously to include not only the $1p$ pickup (^{7}Li, ^{8}Be) channel but also some of the one-nucleon transfer channels, viz., (i) $-1n$ transfer, i.e., (^{7}Li, ^{6}Li) reaction and (ii) $-1p$ transfer, i.e., (^{7}Li, ^{6}He) reaction channels.

The projectile, being weakly bound, and the direct and resonant breakup of ^{7}Li into α and t may play important roles in elastic scattering, which in turn will affect on the $+1p$ transfer channel that we are interested in. The effect of these breakup channels corresponding to different α-t relative angular momenta on elastic scattering has been demonstrated in Fig. 6. The elastic scattering angular distribution calculated using bare CF potential without any breakup or transfer coupling is represented by the dotted line. The calculations with breakup (BU) couplings corresponding to α-t relative angular momentum (i) $L = 0$ (short-dashed line) (ii) $L = 0$ and 1 (dash-dotted line), (iii) $L = 0$, 1, and 2 (medium dashed line), and (iv) $L = 0$, 1, 2, and 3 (dash-dot-dotted line) show that each of these α-t breakup couplings has reduced the elastic scattering cross sections noticeably at backward angles with respect to the uncoupled cross sections (dotted line). It implies that the couplings have generated a repulsive polarization potential contributing to the effective potential for elastic scattering. Comparison between the results with full couplings, i.e., breakup + transfer couplings (solid line) and the ones with all the $\alpha + t$ breakup channels (dash-dot-dotted line) shows that the effect of transfer coupling on elastic scattering is unnoticeable. The calculations with full couplings (solid line) provide a good reproduction of the measured elastic scattering angular distribution which is necessary and important while describing the cross sections for nonelastic

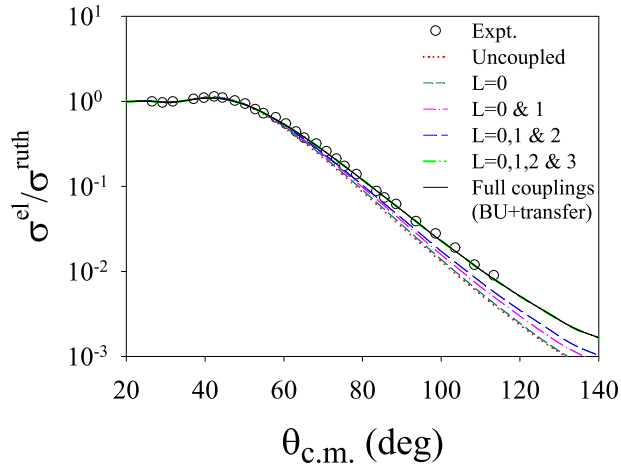

FIG. 6. Measured (circles) elastic scattering cross sections have been compared with the FRESCO calculations (lines) showing the effect of coupling of direct and resonant breakup and transfer channels.

channels simultaneously using the same set of potential and coupling parameters.

For the transfer mass partitions in the CRC+CDCC calculations, only the dominant low-lying excitations of the projectile-like particles and residual target nuclei have been included in the couplings as listed in Table V. All the transfer channels have been coupled to the elastic channel. Only a few channels have been coupled to the bound inelastic state of ^{7}Li (0.478 MeV, $1/2^-$) also. For transfer mass partitions, the real potentials of Woods-Saxon volume form with $V_0 = 25.33$ MeV, $r_0 = 1.185$ fm, and $a_0 = 0.75$ fm, obtained from the optical model fit to the measured elastic scattering angular

TABLE V. Structure information and spectroscopic amplitudes for the overlaps $A = C + x$ corresponding to different states of the nuclei A, C, and x used in the CRC calculations for (^{7}Li,^{6}Li) and (^{7}Li,^{6}He) reactions.

Nucleus (A)	C	x	BE (MeV)	$nlj(x)$	SA
^{7}Li($3/2^-$)	^{6}Li$_{g.s.}$	n	7.251	$1p_{1/2}$	0.690
^{7}Li($1/2^-$)	^{6}Li$_{g.s.}$	n	7.739	$1p_{1/2}$	0.657
^{113}Sn($1/2^+$)	^{112}Sn$_{g.s.}$	n	7.744	$3s_{1/2}$	1.077[45]
^{113}Sn($7/2^+$)	^{112}Sn$_{g.s.}$	n	7.667	$1g_{7/2}$	0.556[45]
^{113}Sn($5/2^+$)	^{112}Sn$_{g.s.}$	n	7.334	$2d_{5/2}$	0.387[45]
^{113}Sn($3/2^+$)	^{112}Sn$_{g.s.}$	n	7.245	$2d_{3/2}$	0.866[45]
^{113}Sn($11/2^-$)	^{112}Sn$_{g.s.}$	n	7.005	$1h_{11/2}$	1.140[45]
^{113}Sn($5/2^+$)	^{112}Sn$_{g.s.}$	n	6.725	$2d_{5/2}$	0.130[45]
^{113}Sn($5/2^+$)	^{112}Sn$_{g.s.}$	n	6.183	$2d_{5/2}$	0.230[45]
^{7}Li($3/2^-$)	^{6}He$_{g.s.}$	p	9.980	$1p_{3/2}$	0.768[46]
^{7}Li($1/2^-$)	^{6}He$_{g.s.}$	p	10.458	$1p_{1/2}$	0.768
^{113}Sb($5/2^+$)	^{112}Sn$_{g.s.}$	p	3.050	$2d_{5/2}$	0.920
^{113}Sb($1/2^+$)	^{112}Sn$_{g.s.}$	p	2.405	$3s_{1/2}$	0.920
^{113}Sb($7/2^+$)	^{112}Sn$_{g.s.}$	p	2.236	$1g_{7/2}$	0.920
^{113}Sb($5/2^+$)	^{112}Sn$_{g.s.}$	p	2.032	$2d_{5/2}$	0.920
^{113}Sb($9/2^+$)	^{112}Sn$_{g.s.}$	p	1.793	$1g_{9/2}$	0.920
^{113}Sb($11/2^-$)	^{112}Sn$_{g.s.}$	p	1.702	$1h_{11/2}$	0.920

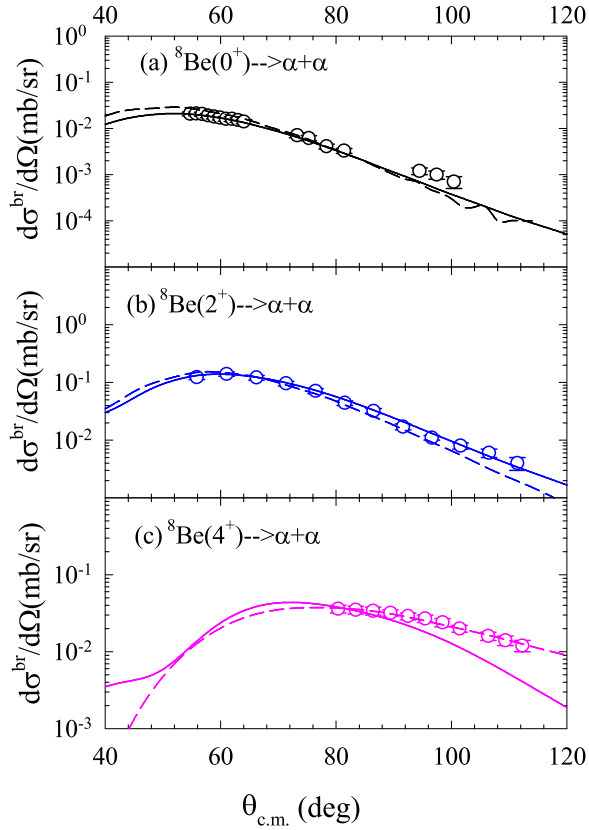

FIG. 7. Experimental and theoretical cross sections for sequential breakup of ^{7}Li → ^{8}Be → $\alpha + \alpha$ corresponding to (a) 0^{+}, (b) 2^{+}, and (c) 4^{+} states of ^{8}Be corresponding to no target excitation. Dashed and solid lines represent the results of FRESCO calculations using CRC only and CDCC+CRC formalisms respectively.

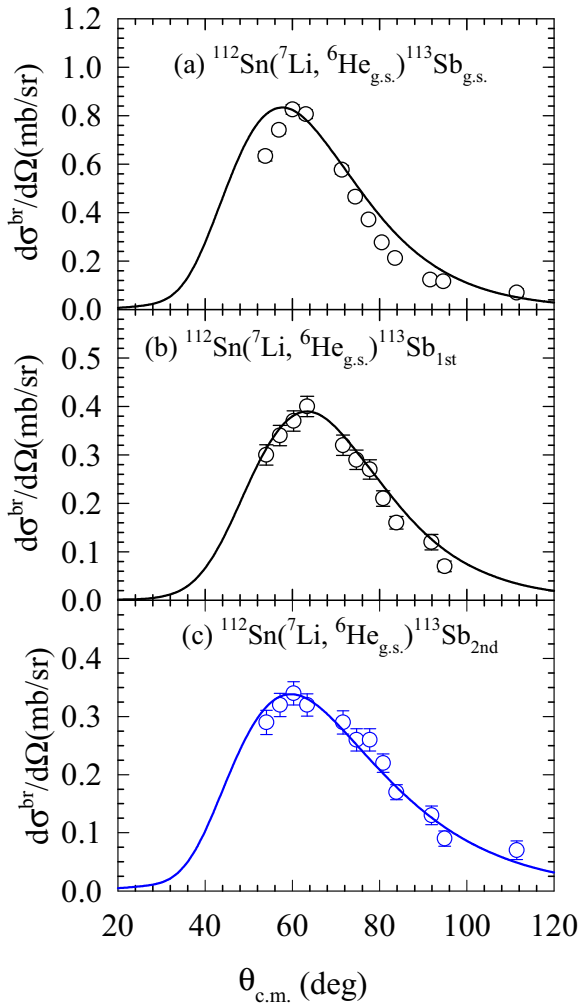

FIG. 8. Experimental cross sections for $1p$ stripping corresponding to g.s. of ^{6}He and (a) g.s., (b) first excited state, and (c) second excited state of ^{113}Sb. Solid lines represent FRESCO calculations using the CDCC+CRC formalism.

distribution, have been used. The imaginary potentials used were of Woods-Saxon square form with $W_0 = 10.0$ MeV, $r_w = 1.0$ fm, and $a_w = 0.63$ fm. For the $+1p$ transfer mass partition, the number of outgoing channels included in the couplings is now reduced compared to the previous(CRC only) calculations due to the limitation in total number of channels that can be included at a time. These channels now correspond to 0^{+}, 2^{+}, and 4^{+} states of ^{8}Be, and ground state $(9/2^{+})$ plus four excited states, i.e., $(1/2^{-}$, 0.537 MeV), $(3/2^{-}$, 0.803 MeV), $(1/2^{+}$, 1.187 MeV), and $(5/2^{+}$, 2.212 MeV) states of ^{111}In. The spectroscopic amplitudes used are same as those given in Table II.

For the $-1n$ and $-1p$ transfer mass partitions, the number of outgoing channels included in the couplings are seven and six, respectively. The details of these two transfer channels including the spectroscopic amplitudes and structure information on the states included in the couplings are given in Table V.

In order to verify that the potentials and coupling parameters used for the elastic and transfer channels in the CDCC + CRC formalism are realistic, the calculated cross sections have been compared with the experimental data not only for ^{8}Be breakup but also for a few representative states corresponding to other transfer reactions. The cross sections for (^{7}Li,^{8}Be → $\alpha + \alpha$) reaction calculated from the CDCC + CRC formalism were found to compare very well with the ones calculated from the CRC only formalism as well as the experimental data, as shown in Fig. 7.

Typical $-1p$ transfer cross sections calculated from the CDCC + CRC calculations (solid lines) corresponding to g.s., first excited state, and second excited state of ^{113}Sb are shown in Figs. 8(a), 8(b), and 8(c) respectively. Similarly, for $-1n$ transfer reactions, the cross sections obtained from the CDCC + CRC calculations (solid lines) are shown in Figs. 9(a) and 9(b) corresponding to g.s. and 0.738-MeV excited state of ^{113}Sn respectively. The calculations are found to reproduce the measured data (hollow circles) reasonably well. This implies that the parameters used in the coupled-channels calculations are realistic, by which it has been possible to describe elastic scattering and several transfer channels simultaneously through a single coupled-channels calculation.

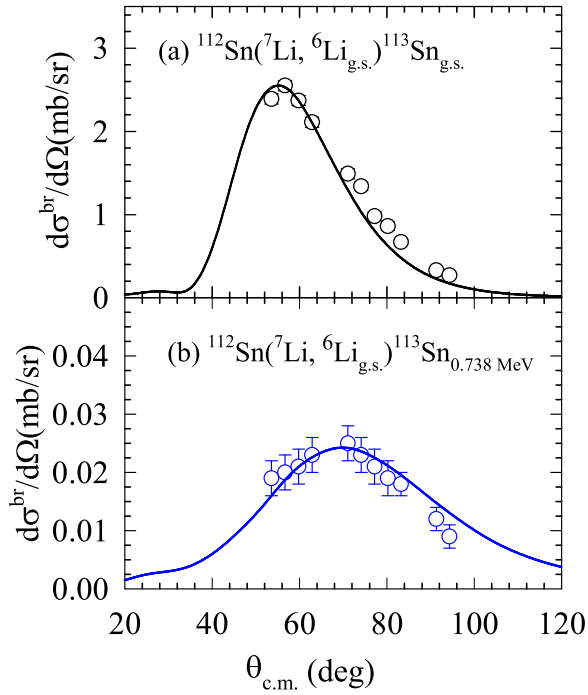

FIG. 9. Experimental cross sections for $1n$ stripping corresponding to g.s. of ^{6}Li and (a) g.s. and (b) 0.738-MeV excited state of ^{113}Sn. Solid lines represent FRESCO calculations using CDCC+CRC formalism.

VI. SUMMARY

In summary, we have presented new results for α-α coincidence measurements following proton pickup by ^{7}Li from the ^{112}Sn target at an energy above the Coulomb barrier ($E_{cm}/V_b \sim 1.37$) using a large detector array (with a maximum angular coverage of $\theta_{12} \sim 93^{\circ}$) of Si strip detectors. The relative energy distributions of the coincident α-α events and Monte Carlo simulations confirm the observation of ^{8}Be breakup through its 4^{+} resonance state for the first time along with already known 0^{+} and 2^{+} states.

Exclusive breakup cross sections for three resonance states of ^{8}Be have been obtained and compared with the CRC calculations. A simultaneous description of elastic, $-1n$ transfer, $-1p$ transfer, and $+1p$ transfer channels has also been attempted using the same set of potential and coupling parameters. The effect of $\alpha + t$ breakup and transfer couplings on elastic scattering has been investigated. The couplings of $\alpha + t$ breakup channels corresponding to the states with the α-t relative angular momentum L (= 0, 1, 2, 3) are found to increase the elastic scattering at backward angles, though the effect of $L = 3$ is most dominant. The effect of transfer coupling on elastic scattering is found to be negligible. The results of the coupled-channels calculations using the CDCC + CRC formalism are found to reproduce simultaneously the experimental cross sections for elastic scattering, transfer, and breakup reactions.

The detailed study of $1p$ transfer-induced breakup into 2α via different resonant states including the one at very high excitation (11.3 MeV) of ^{8}Be presented here provides a good foundation for understanding the reaction mechanisms of total α production and the sequential modes of projectile breakup.

ACKNOWLEDGMENTS

The financial support of BRNS, DAE (IN) through the Project No. 2012/21/11-BRNS/1090 is greatly acknowledged.

[1] J. J. Kolata, V. Guimaraes, and E. F. Aguilera, Eur. Phys. J. A **52**, 123 (2016).
[2] L. Canto, P. Gomes, R. Donangelo, J. Lubian, and M. Hussein, Phys. Rep. **596**, 1 (2015).
[3] B. B. Back, H. Esbensen, C. L. Jiang, and K. E. Rehm, Rev. Mod. Phys. **86**, 317 (2014).
[4] N. Keeley, N. Alamanos, K. Kemper, and K. Rusek, Prog. Part. Nucl. Phys. **63**, 396 (2009).
[5] N. Keeley, R. Raabe, N. Alamanos, and J. L. Sida, Prog. Part. Nucl. Phys. **59**, 579 (2007).
[6] L. F. Canto, P. R. S. Gomes, R. Donangelo, and M. S. Hussein, Phys. Rep. **424**, 1 (2006).
[7] S. Santra, S. Kailas, V. V. Parkar, K. Ramachandran, V. Jha, A. Chatterjee, P. K. Rath, and A. Parihari, Phys. Rev. C **85**, 014612 (2012).
[8] G. R. Kelly, N. J. Davis, R. P. Ward, B. R. Fulton, G. Tungate, N. Keeley, K. Rusek, E. E. Bartosz, P. D. Cathers, D. D. Caussyn *et al.*, Phys. Rev. C **63**, 024601 (2000).
[9] C. Signorini, M. Mazzocco, G. Prete, F. Soramel, L. Stroe, A. Andrighetto, I. Thompson, A. Vitturi, A. Brondi, M. Cinausero *et al.*, Eur. Phys. J. A **10**, 249 (2001).
[10] R. J. Woolliscroft, N. M. Clarke, B. R. Fulton, R. L. Cowin, M. Dasgupta, D. J. Hinde, C. R. Morton, and A. C. Berriman, Phys. Rev. C **68**, 014611 (2003).
[11] C. Signorini, A. Edifizi, M. Mazzocco, M. Lunardon, D. Fabris, A. Vitturi, P. Scopel, F. Soramel, L. Stroe, G. Prete *et al.*, Phys. Rev. C **67**, 044607 (2003).
[12] K. O. Pfeiffer, E. Speth, and K. Bethge, Nucl. Phys. A **206**, 545 (1973).
[13] A. Pakou, N. Alamanos, A. Gillibert, M. Kokkoris, S. Kossionides, A. Lagoyannis, N. G. Nicolis, C. Papachristodoulou, D. Patiris, and D. Pierroutsakou, Phys. Rev. Lett. **90**, 202701 (2003).
[14] H. Kumawat, V. Jha, V. V. Parkar, B. J. Roy, S. Santra, V. Kumar, D. Dutta, P. Shukla, L. M. Pant, A. K. Mohanty *et al.*, Phys. Rev. C **81**, 054601 (2010).
[15] F. Souza, C. Beck, N. Carlin, N. Keeley, R. L. Neto, M. de Moura, M. Munhoz, M. D. Santo, A. Suaide, E. Szanto *et al.*, Nucl. Phys. A **821**, 36 (2009).
[16] F. Souza, N. Carlin, C. Beck, N. Keeley, A. Diaz-Torres, R. L. Neto, C. Siqueira-Mello, M. M. de Moura, M. G. Munhoz, R. A. N. Oliveira *et al.*, Eur. Phys. J. A **44**, 181 (2010).

[17] F. Souza, N. Carlin, C. Beck, N. Keeley, A. Diaz-Torres, R. L. Neto, C. Siqueira-Mello, M. de Moura, M. Munhoz, R. Oliveira *et al.*, Nucl. Phys. A **834**, 420c (2010).
[18] K. Hagino, A. Vitturi, C. H. Dasso, and S. M. Lenzi, Phys. Rev. C **61**, 037602 (2000).
[19] A. Diaz-Torres, I. J. Thompson, and C. Beck, Phys. Rev. C **68**, 044607 (2003).
[20] A. Shrivastava, A. Navin, N. Keeley, K. Mahata, K. Ramachandran, V. Nanal, V. Parkar, A. Chatterjee, and S. Kailas, Phys. Lett. B **633**, 463 (2006).
[21] P. K. Rath, S. Santra, N. L. Singh, R. Tripathi, V. V. Parkar, B. K. Nayak, K. Mahata, R. Palit, S. Kumar, S. Mukherjee *et al.*, Phys. Rev. C **79**, 051601(R) (2009).
[22] P. K. Rath, S. Santra, N. L. Singh, B. K. Nayak, K. Mahata, R. Palit, K. Ramachandran, S. K. Pandit, A. Parihari, A. Pal *et al.*, Phys. Rev. C **88**, 044617 (2013).
[23] M. Dasgupta, D. J. Hinde, R. D. Butt, R. M. Anjos, A. C. Berriman, N. Carlin, P. R. S. Gomes, C. R. Morton, J. O. Newton, A. S. de Toledo *et al.*, Phys. Rev. Lett. **82**, 1395 (1999).
[24] M. Dasgupta, D. J. Hinde, K. Hagino, S. B. Moraes, P. R. S. Gomes, R. M. Anjos, R. D. Butt, A. C. Berriman, N. Carlin, C. R. Morton *et al.*, Phys. Rev. C **66**, 041602(R) (2002).
[25] D. H. Luong, M. Dasgupta, D. J. Hinde, R. du Rietz, R. Rafiei, C. J. Lin, M. Evers, and A. Diaz-Torres, Phys. Rev. C **88**, 034609 (2013).
[26] S. Santra, V. V. Parkar, K. Ramachandran, U. K. Pal, A. Shivastava, B. J. Roy, B. K. Nayak, A. Chatterjee, R. K. Choudhury, and S. Kailas, Phys. Lett. B **677**, 139 (2009).
[27] D. Chattopadhyay, S. Santra, A. Pal, A. Kundu, K. Ramachandran, R. Tripathi, D. Sarkar, S. Sodaye, B. K. Nayak, A. Saxena *et al.*, Phys. Rev. C **94**, 061602(R) (2016).
[28] S. K. Pandit, A. Shrivastava, K. Mahata, N. Keeley, V. V. Parkar, P. C. Rout, K. Ramachandran, I. Martel, C. S. Palshetkar, A. Kumar *et al.*, Phys. Rev. C **93**, 061602(R) (2016).
[29] R. Rafiei, R. du Rietz, D. H. Luong, D. J. Hinde, M. Dasgupta, M. Evers, and A. Diaz-Torres, Phys. Rev. C **81**, 024601 (2010).
[30] E. C. Simpson, K. J. Cook, D. H. Luong, S. Kalkal, I. P. Carter, M. Dasgupta, D. J. Hinde, and E. Williams, Phys. Rev. C **93**, 024605 (2016).
[31] K. J. Cook, E. C. Simpson, D. H. Luong, S. Kalkal, M. Dasgupta, and D. J. Hinde, Phys. Rev. C **93**, 064604 (2016).
[32] D. Chattopadhyay, S. Santra, A. Pal, A. Kundu, K. Ramachandran, R. Tripathi, B. J. Roy, T. Nag, Y. Sawant, B. K. Nayak *et al.*, Phys. Rev. C **97**, 051601(R) (2018).
[33] C. Beck, Nucl. Phys. A **834**, 440c (2010).
[34] C. Beck, N. Keeley, and A. Diaz-Torres, Phys. Rev. C **75**, 054605 (2007).
[35] P. E. F. Carnelli, D. M. Heimann, A. J. Pacheco, A. Arazi, O. A. Capurro, J. O. F. Niello, M. A. Cardona, E. de Barbara, J. M. Figueira, D. L. Hojman *et al.*, Nucl. Phys. A **969**, 94 (2018).
[36] V. M. Datar, D. R. Chakrabarty, S. Kumar, V. Nanal, S. Pastore, R. B. Wiringa, S. P. Behera, A. Chatterjee, D. Jenkins, C. J. Lister *et al.*, Phys. Rev. Lett. **111**, 062502 (2013).
[37] F. C. Barker, Aus. J. Phys. **41**, 743 (1988).
[38] R. J. de Meijer and R. Kamermans, Rev. Mod. Phys. **57**, 147 (1985).
[39] D. R. Tilley, J. H. Kelley, J. L. Godwin, D. J. Millener, J. E. Purcell, C. G. Sheu, and H. R. Weller, Nucl. Phys. A **745**, 155 (2004).
[40] I. J. Thompson, Comput. Phys. Rep. **7**, 167 (1988).
[41] L. C. Chamon, B. V. Carlson, L. R. Gasques, D. Pereira, C. D. Conti, M. A. G. Alvarez, M. S. Hussein, M. A. C. Ribeiro, J. E. S. Rossi, and C. P. Silva, Phys. Rev. C **66**, 014610 (2002).
[42] M. Avrigeanu and V. Avrigeanu, Phys. Rev. C **73**, 038801 (2006).
[43] X. Li, C. Liang, and C. Cai, Nucl. Phys. A **789**, 103 (2007).
[44] B. Buck and A. C. Merchant, J. Phys. G: Nucl. Part. Phys. **14**, L211 (1988).
[45] E. J. Schneid, A. Prakash, and B. L. Cohen, Phys. Rev. **156**, 1316 (1967).
[46] S. Cohen and D. Kurath, Nucl. Phys. A **101**, 1 (1967).